JACS
JOURNAL OF THE AMERICAN CHEMICAL SOCIETY
Article
pubs.acs.org/JACS

Hidden Non-Innocence in an Expanded Porphyrin: Electronic Structure of the Siamese-Twin Porphyrin's Dicopper Complex in Different Oxidation States

Lina K. Blusch,[†] Kathryn E. Craigo,[§] Vlad Martin-Diaconescu,[‡] Ashley B. McQuarters,[§] Eckhard Bill,[‡] Sebastian Dechert,[†] Serena DeBeer,*[,‡,∥] Nicolai Lehnert,*[,§] and Franc Meyer*[,†]

[†]Institut für Anorganische Chemie, Georg-August-Universität, Tammannstr. 4, 37077 Göttingen, Germany
[‡]MPI für Chemische Energiekonversion, Stiftstraße 34-36, 45470 Mülheim an der Ruhr, Germany
[§]Department of Chemistry, University of Michigan, Ann Arbor, Michigan 48109-1055, United States
[∥]Department of Chemistry and Chemical Biology, Cornell University, Ithaca, New York 14853, United States

Supporting Information

ABSTRACT: The Siamese-twin porphyrin ($\mathbf{2H_4}$) is a unique pyrazole-expanded porphyrin providing two adjacent cavities each offering an $\{N_4\}$ binding motif. It was previously found to form stable dicopper(II) or dinickel(II) complexes where both metal ions are nested in a porphyrin-like environment. This work addresses the rich redox chemistry of the dicopper complex $\mathbf{2Cu_2}$ that originates from the redox synergy of two proximate metal ions in combination with the potentially non-innocent expanded porphyrin ligand. Complementing previous X-ray crystallographic and SQUID data for solid material, the electronic structure of parent $\mathbf{2Cu_2}$ in solution was now investigated by MCD and EPR spectroscopy. This allowed the assignment of UV−vis absorptions and confirmed the drastic twist of the molecule with ferromagnetically coupled copper(II) ions. $\mathbf{2Cu_2}$ was found to exhibit multiple redox events in the potential range from −2.4 to +1.7 V versus Fc/Fc^+, and singly oxidized $[\mathbf{2Cu_2}]^+$ as well as doubly oxidized $[\mathbf{2Cu_2}]^{2+}$ were characterized in detail by various analytical and spectroscopic methods. $[\mathbf{2Cu_2}]^+$ was found by EPR spectroscopy and DFT calculations to have an $S = 1/2$ ground state, while $[\mathbf{2Cu_2}]^{2+}$ is diamagnetic. Single crystal X-ray crystallography of $[\mathbf{2Cu_2}(acetone)_2](BF_4)_2$ revealed that the $\mathbf{2Cu_2}$ core is structurally invariant upon two-fold oxidation, while XAS measurements at the Cu *K*-edge for $\mathbf{2Cu_2}$ and $[\mathbf{2Cu_2}(acetone)_2](BF_4)_2$ showed that the copper ions remain in the +2 oxidation state throughout. The combined experimental and computational evidence identified the Siamese-twin porphyrin as a multi-electron redox-active ligand with hidden non-innocence. Each ligand subunit upon oxidation forms a ligand-centered radical, though the spin vanishes because of covalency and strong antiferromagnetic coupling between the ligand radical and the proximate metal ion. Complexes of the Siamese-twin porphyrin may thus serve as a valuable bioinspired platform that combines both metal−ligand and two-metal-ion cooperativities for use in multi-electron processes.

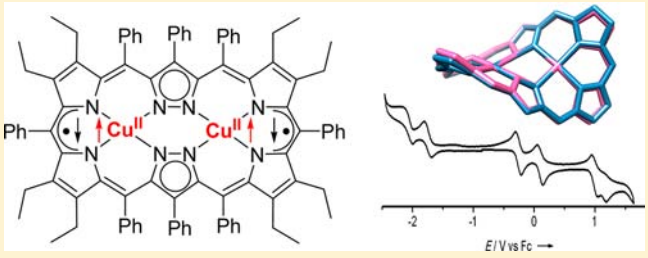

INTRODUCTION

Porphyrins are non-innocent ligand systems that give cationic π-radicals upon a one-electron oxidation.[1] In nature this is extensively exploited in, e.g., heme catalysis[2] or photosynthesis.[3] Synthetic porphyrins, such as tetraphenylporphyrin, usually show four distinct redox steps,[4] namely, two oxidative and two reductive processes all located on the porphyrin ligand itself. The binding of redox-active metals can further enrich these properties and often results in a multitude of reversible one-electron redox processes.[5]

Expanded porphyrins are higher analogues of porphyrins that contain more than four pyrrole or pyrrole-like units within the macrocycle.[6] They usually have extended π-systems, and oxidation may be facilitated as reflected by red-shifted absorption bands.[6,7] Some expanded porphyrins, because of their larger ring size, are capable of hosting two proximate metal ions;[8] in cases where these are redox active, the overall redox sequence may be even more multifaceted than for porphyrins and their mononuclear complexes.[9] However, few studies have yet addressed in detail the redox processes and redox sites in expanded porphyrins.[9,10]

A prominent expanded porphyrin scaffold is [28]hexaphyrin that can be chemically oxidized to [26]hexaphyrin **1** (Scheme 1), which is associated with a switch from Möbius to Hückel aromaticity.[11] The metalation of expanded porphyrins, such as hexaphyrin **1** and its N-confused isomer, is versatile, though not always predictable.[6b] For example, in homobimetallic complexes of **1** two Au^{III} are found with an $\{N_2C_2\}$ donor set,[12] while two Hg^{II} were observed binding in an $\{N_2C\}$ fashion.[13]

Received: June 19, 2013
Published: August 15, 2013

   dx.doi.org/10.1021/ja406176e | J. Am. Chem. Soc. 2013, 135, 13892−13899

Scheme 1. [26]Hexaphyrin(1.1.1.1.1.1) and the Siamese-Twin Porphyrin Scaffold

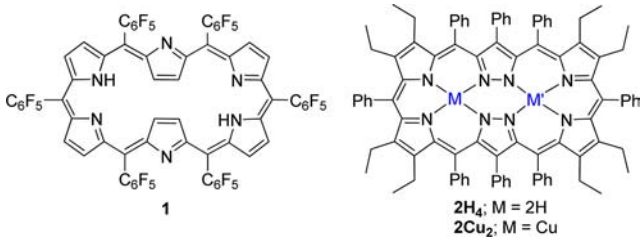

Metalation with first-row transition metals, such as copper, is usually accompanied by ligand oxygenation at the meso positions of **1** and concomitant dearomatization.[14] N-confused hexaphyrins are prone to C-oxygenation at the inverted ring, thus providing $\{N_3O\}$ cavities for metal binding.[15]

Recently we introduced the Siamese-twin porphyrin $\mathbf{2H_4}$ (Scheme 1), which represents the first expanded porphyrin incorporating pyrazole units in its framework.[16] Its design resembles two joined porphyrins with adjacent cavities each offering an $\{N_4\}$ binding motif.[16,17] Indeed the Siamese-twin prophyrin was shown to form stable dicopper(II) and dinickel(II) complexes. Given the presence of two porphyrin-like subunits, rich redox chemistry was anticipated from the ensemble of potential ligand non-innocence and two proximate metal centers. Here we report, as a representative example, a detailed investigation of the redox properties of the dicopper complex $\mathbf{2Cu_2}$, which establishes the Siamese-twin porphyrin as a multi-electron non-innocent ligand platform. We show that this unusual system can shuttle through several oxidation states with ligand non-innocence hidden from X-ray crystallography.[18]

RESULTS AND DISCUSSION

To provide a solid basis for describing the oxidized species of $\mathbf{2Cu_2}$, a thorough analysis of the electronic structure of this dicopper(II) complex was needed first. $\mathbf{2Cu_2}$ was previously investigated in solid state by X-ray analysis and SQUID magnetometry (see SI), which revealed a highly twisted helical structure (similar to the free-base $\mathbf{2H_4}$)[17] with copper(II) in roughly square-planar coordination environment but with unusual ferromagnetic coupling of the d^9 (S = 1/2) metal ions because of an almost orthogonal orientation of their two magnetic orbitals (J = +16.3 cm^{-1}).[16] To confirm the intramolecular nature of the coupling, $\mathbf{2Cu_2}$ was further investigated by electron paramagnetic resonance (EPR) measurements of a frozen-solution sample (Figure 1). The X-band spectrum recorded at 10 K corroborates the postulated triplet ground state since it shows wide split signals at g = 2 with distinct zero-field splitting from dipole interaction and significant half-field signals from transitions between the m_s = ±1 levels at g = 4. The half-field signal exhibits well resolved hyperfine splitting from interaction with both Cu nuclei, which is even the most dominant feature of the spectrum recorded in parallel-mode ($B_1 \| B_0$, inset of Figure 1). Both spectra could be simulated by assuming a spin pair with anisotropic dipole interaction of S_1 = 1/2 and S_2 = 1/2 in addition to the ferromagnetic isotropic exchange coupling detected by SQUID (J = +16.3 cm^{-1}). The **g**- and **A**-tensor for the Cu sites had to be twisted for the EPR simulations, according to a 90° rotation for S_2 around the x-axis, which is close to the angle found for the twist of coordination sites in the crystal structure (80°).

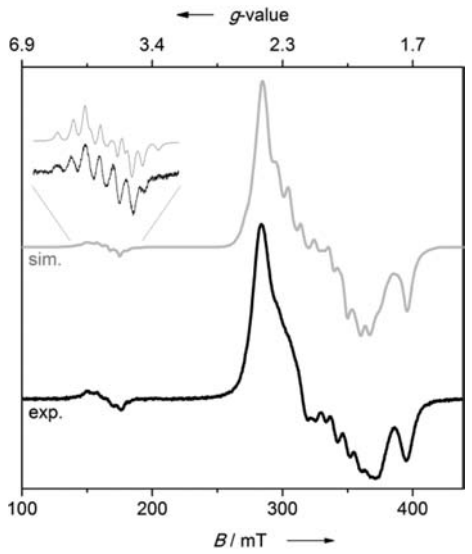

Figure 1. X-band EPR spectra of $\mathbf{2Cu_2}$ in CH_2Cl_2 recorded at 10 K with $B_1 \perp B_0$ and $B_1 \| B_0$ (inset) are shown in black. Given in gray are simulations with g_x = 2.03, g_y = 2.07, g_z = 2.13 and a_z = 220 × 10^{-4} cm^{-1} for both Cu sites and x-rotation angles 90° and 80° for **g** and **A** of Cu_2.

From the value of the dipole interaction obtained from parameter optimization, J_d = (251, 442, −694)·10^{-4} cm^{-1}, a mean spin−spin distance of 3.8 Å was determined for the Cu(II) pair. This interpretation was based on an 8-point dipole model with 25% of a spin centered on each of the four lobes of the two $d_{x^2-y^2}$ magnetic orbitals. Interestingly, the twist of the Cu sites also explains nicely the rhombicity of J_d. In summary, twist angle and distance of the spin density distributions agree well with the molecular structure found for the solid material (d(Cu···Cu) = 3.88 Å), thus indicating persistence of the structure in solution and localization of the spin densities on the metal ions.

Figure 2 shows a comparison of the UV−vis absorption and low-temperature magnetic circular dichroism (MCD) spectrum of $\mathbf{2Cu_2}$ along with a correlated fit of these data. The MCD spectrum features a significant (temperature dependent; see Figure S3) C-term intensity, supporting a spin-degenerate

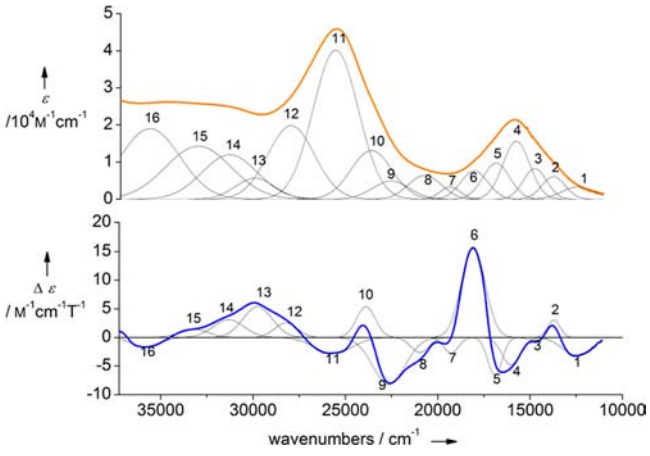

Figure 2. UV−vis spectrum of $\mathbf{2Cu_2}$ (orange, top) and MCD spectrum at 4 K (blue, bottom), and deconvolution into the different subspectra using the program Peakfit.

dx.doi.org/10.1021/ja406176e | J. Am. Chem. Soc. 2013, 135, 13892−13899

triplet ground state for $\mathbf{2Cu_2}$ that is confirmed by comparison of variable temperature and variable field MCD data with calculated Brillouin curves (Figure S4). The C-term spectrum of $\mathbf{2Cu_2}$ allowed us to resolve the broad bands observed in the UV−vis spectrum into sixteen different electronic transitions within the measured region (Table S1). Surprisingly, the two main absorption bands in the UV−vis spectrum, 4 and 11 (see Figure 2), do not show much MCD intensity. This points to pure, ligand-derived electronic transitions, most likely $\pi \rightarrow \pi^*$ transitions, that lack any degeneracy in the excited state and any significant metal contribution. This is in stark contrast to the Soret and Q bands of porphyrins[19] and reflects the low symmetry and twisted structure of $\mathbf{2Cu_2}$. TD-DFT calculations were used to gain further insight into the nature of the electronic transitions observed in the optical spectra of $\mathbf{2Cu_2}$ (see SI for details). The HOMO−LUMO region of the MO diagram of $\mathbf{2Cu_2}$ is dominated by π and π^* orbitals of the macrocyclic ligand. Because of the low symmetry and the severe distortion of the macrocycle, the π-interaction along the conjugated system is reduced, leading to a large number of π and π^* MOs with very similar energies that dominate the HOMO−LUMO region of the complex. Correspondingly, the TD-DFT calculations predict that (inner-ligand) $\pi \rightarrow \pi^*$ transitions are distributed over the whole vis-NIR range and that these transitions make major contributions to the absorption spectrum. However, these transitions should not have much C-term intensity in the MCD spectrum. Correspondingly, the MCD spectrum in Figure 2 shows quite weak C-term features with molar intensities below |20| M^{-1} cm^{-1} T^{-1}. These molar intensities are very small compared to metalloporphyrins, which can reach into the thousands M^{-1} cm^{-1} T^{-1} for the Soret transition.[20] On the other hand, the TD-DFT calculations predict a number of $\pi \rightarrow d_{x^2-y^2}$ ligand-to-metal CT (LMCT) transitions in the 10 000−17 000 cm^{-1} region for $\mathbf{2Cu_2}$, which have smaller oscillator strengths, but the energy pattern of which (see Table S2) matches the MCD spectrum (Figure 2, bottom) almost perfectly. Based on this finding, bands 1−5 observed by MCD are assigned to $\pi \rightarrow d_{x^2-y^2}$ LMCT transitions, which, due to their significant metal contribution, should be quite intense in the MCD spectrum. Additionally, the TD-DFT calculations predict the occurrence of d−d transitions above 18 000 cm^{-1}, and in particular band 6, which is very intense in MCD, is assigned to a combination of d−d and $\pi \rightarrow d_{x^2-y^2}$ LMCT transitions. Similar assignments are made for bands 7−10 (see Table S2). As mentioned above, it is likely that in the UV−vis spectrum additional contributions to the intensity arise from $\pi \rightarrow \pi^*$ transitions in agreement with the TD-DFT results. The higher energy region of the spectrum above 25 000 cm^{-1}, including bands 11 and 12, is dominated by $\pi \rightarrow \pi^*$ transitions of the macrocycle.

Having established that the HOMO−LUMO region of $\mathbf{2Cu_2}$ is dominated by π and π^* orbitals of the Siamese-twin porphyrin ligand, redox properties of $\mathbf{2Cu_2}$ were investigated electrochemically using cyclic and square wave voltammetry (CV and SWV; Figures 3, S6, and S7). A sequence of six redox steps (coming in three pairs a, b, and c) is observed, four of which seem to be electrochemically reversible with half wave potentials $E_{1/2}$ = −1.75, −0.26, +0.09, and +0.99 V (versus ferrocene). Two further processes have peak potentials E_p^{ox} at −2.00 and +1.18 V. SWV suggests that all waves correspond to one-electron processes. High distortion and electron-donating substituents are known to destabilize the HOMO and with that facilitate the oxidation which occurs already at a slightly

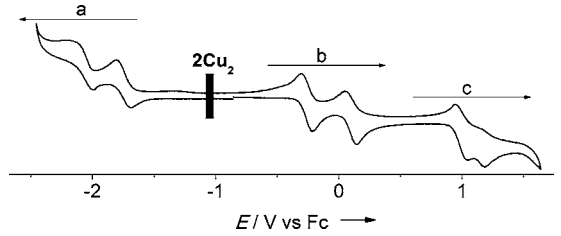

Figure 3. CV curve of $\mathbf{2Cu_2}$ in CH_2Cl_2 with $[NBu_4]PF_6$ as an electrolyte at a scan rate of 100 mV s^{-1} vs ferrocene (Fc) as internal standard.

negative potential.[21] However, the free ligand $\mathbf{2H_4}$ itself shows only irreversible redox processes of little diagnostic value (Figure S8).

Bulk electrolysis is not limited to the barrier layer, and thus in situ UV−vis spectra were constantly recorded during electrochemical reduction (pair a) and oxidation (pairs b and c) of $\mathbf{2Cu_2}$ (Figures 4 and S9). Subsequent reoxidation or

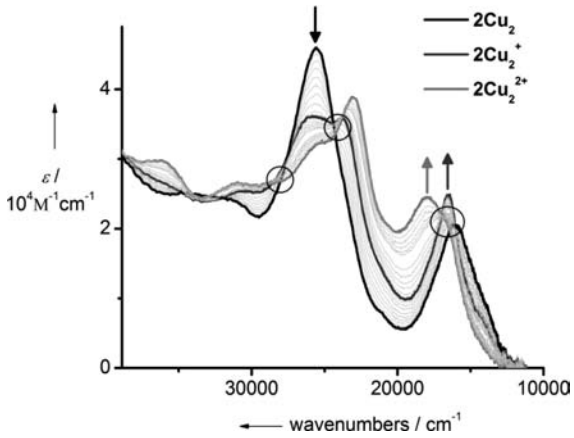

Figure 4. UV−vis spectra recorded during electrochemical oxidation in CH_2Cl_2, UV−vis spectra of $\mathbf{2Cu_2}$, $[\mathbf{2Cu_2}]^+$, and $[\mathbf{2Cu_2}]^{2+}$ are highlighted. Isosbestic points are indicated via black circles.

rereduction, respectively, and comparison of the UV−vis spectra revealed that, after several redox cycles, only the conversions of pair b were found to be fully chemically reversible. Pair b represents the sequential oxidation from $\mathbf{2Cu_2}$ (bluish-green) to $[\mathbf{2Cu_2}]^+$ (green) and $[\mathbf{2Cu_2}]^{2+}$ (brown) (Figure S10). The main absorption band of $\mathbf{2Cu_2}$ at 25 575 cm^{-1} decreases, and λ_{max} is blue-shifted from 15 898 cm^{-1} to 16 529 cm^{-1} during the first oxidation and further blue-shifted to 17 986 (with a shoulder at 16 863 cm^{-1}) upon generation of $[\mathbf{2Cu_2}]^{2+}$; the main absorption is then observed at 23 095 cm^{-1}. Isosbestic points indicate direct conversions.

A comproportionation constant $K_c = 9.5 \times 10^5$ for $[\mathbf{2Cu_2}]^+$ was calculated,[22] reflecting thermodynamic stability of the mixed-valent species. Titration of $\mathbf{2Cu_2}$ in CH_2Cl_2 with a 0.1 M nitroethane solution of $AgBF_4$, followed by UV−vis spectroscopy, showed a very similar development of the absorption spectra (Figure S11). The spectrum of $[\mathbf{2Cu_2}]^{2+}$ was reached after adding 2 equiv of $AgBF_4$, confirming that each redox wave of b corresponds to a one-electron oxidation. Using chemical oxidation with $AgBF_4$, $[\mathbf{2Cu_2}]^+$ and $[\mathbf{2Cu_2}]^{2+}$ could also be isolated in pure form and close to quantitative yields.

Oxidation of $\mathbf{2Cu_2}$ raises the question where oxidation takes place in such system that has a potentially redox-active

bicompartmental ligand and two Cu^{II} ions. Singly oxidized $[\mathbf{2Cu_2}]^+$ has a spin $S = 1/2$ ground state; its EPR spectrum shows an almost axial signal with $g_x \approx g_y = 2.03, 2.07$ and $g_z = 2.18$, and with the typical $^{63/65}Cu$ ($I = 3/2$) hyperfine splitting of 190×10^{-4} cm^{-1} in g_z direction, which is characteristic of tetragonal Cu^{II} (Figure 5). The nine-line pattern at g_x and g_y

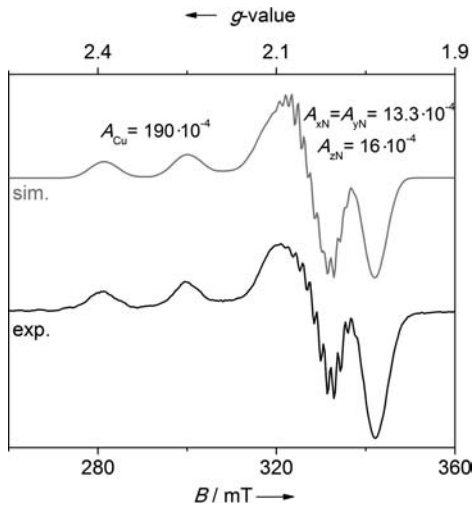

Figure 5. EPR spectrum of $[\mathbf{2Cu_2}]^+$ at 166 K in CH_2Cl_2 and its simulation in gray with $g_x = 2.03$, $g_y = 2.07$, $g_z = 2.18$. Hyperfine coupling constants are given in the figure in $[cm^{-1}]$.

originates from superhyperfine coupling to the four nitrogen atoms located in the *x,y* plane, in accord with the unpaired electron residing in the $d_{x^2-y^2}$ orbital. However, this does not reveal the site of oxidation, since both a single metal-centered oxidation (giving $[\mathbf{2Cu^{II}Cu^{III}}]^+$ with low-spin Cu^{III}) as well as a ligand-centered oxidation with strong antiferromagnetic coupling of the radical and one of the Cu^{II} ions (namely, $[(\mathbf{2^{\bullet}Cu^{II}})\mathbf{Cu^{II}}]^+$) or to a pair of ferromagnetically coupled Cu^{II} ions (namely, $[(\mathbf{2^{\bullet}(Cu^{II}Cu^{II})})]^+$) would give rise to a remaining Cu-centered $S = 1/2$ system. One should note that antiferromagnetic coupling between a cationic π-radical and Cu^{II} was observed in distorted porphyrin complexes,[23] whereas the isolation of a Cu^{III} porphyrinic core is still pending. In any case the EPR spectrum of mixed-valent $[\mathbf{2Cu_2}]^+$ evidences the electron to be localized on one side of the ligand on the EPR time scale (class I behavior; see Figure S12 for variable temperature EPR spectra), since hyperfine coupling to only one of the Cu nuclei is observed instead of a seven line pattern originating from a coupling to two copper ions. Only a very broad and weak electronic absorption in the NIR region, where metal-to-metal or ligand-to-ligand intervalence charge-transfer (IVCT) transitions might be expected, is discernible for $[\mathbf{2Cu_2}]BF_4$ but is of little diagnostic value (Figure S13).

DFT calculations helped to shed light on the electronic structure of $[\mathbf{2Cu_2}]^+$. We first optimized the structure of $\mathbf{2Cu_2}$ for the triplet, broken-symmetry singlet, and closed-shell singlet state (see SI). B3LYP/TZVP single point calculations on these structures predict the ground state to be the triplet state, in agreement with experiment (spin density plot shown in Figure S21). Analysis of the triplet wave function shows that the bonds between the copper(II) centers in $\mathbf{2Cu_2}$ and the nitrogen donors of the Siamese twin porphyrin are very covalent (likely overestimated in the calculations), with spin densities of about +0.5 on each of the copper centers and about +1.0 on the ligand (see also Table S4). The coupling constant, *J*, is calculated to be $+67$ cm^{-1} ($H = -2J \cdot S_A \cdot S_B$). Interestingly, one-electron oxidation of the complex from $\mathbf{2Cu_2}$ ($S = 1$) to $[\mathbf{2Cu_2}]^+$ ($S = 3/2$) does not change the spin densities on the copper centers at all but increases the spin on the ligand from +0.9 to +1.9, which shows that this oxidation is purely ligand based (calculated with B3LYP/6-311G* on the optimized triplet structure of $\mathbf{2Cu_2}$; see Table S4); this is further illustrated in Figures S22 and S23. Experimentally, $[\mathbf{2Cu_2}]^+$ shows an $S = 1/2$ ground state, so we reconverged the wave function for this complex for the broken-symmetry $S = 1/2$ state. In this case, the spin densities on the copper centers are again invariant, but the spin density on the ligand has vanished (see Figure S24 and Table S4). Further inspection of the calculated wave function shows that this is due to the fact that positive (from covalency) and negative (from ligand oxidation) spin densities now compensate each other. Hence, the DFT calculations confirm that in $[\mathbf{2Cu_2}]^+$ the ligand is oxidized to a monoradical, while the copper remains in the +2 oxidation state. In summary, the DFT calculations predict that the copper centers in $[\mathbf{2Cu_2}]^+$ are ferromagnetically coupled to each other ($S = 1$) and then antiferromagnetically coupled to a delocalized ligand radical, resulting in the total spin of $S = 1/2$. However, such delocalized electronic structure is not in agreement with the EPR results, which point toward a non-delocalized radical nature of $[\mathbf{2Cu_2}]^+$. This indicates that DFT overemphasizes the delocalization of the ligand radical in our Siamese-twin porphyrin complexes, in agreement with the general tendency of DFT to favor electron delocalization. Taking into account the EPR results, we conclude that $[(\mathbf{2^{\bullet}Cu^{II}})\mathbf{Cu^{II}}]^+$ is the proper electronic description.

The twice oxidized species $[\mathbf{2Cu_2}]^{2+}$ is EPR-silent at X-band, suggesting a diamagnetic ground state (or a large zero-field splitting in case of $S > 1/2$); well-resolved NMR resonances at room temperature clearly evidence diamagnetism (Figures S14–S17). One quarter of the molecule is magnetically inequivalent because of its D_2 symmetry in solution. The $S = 0$ ground state is compatible either with a two-fold metal-centered oxidation (giving $[\mathbf{2Cu^{III}}_2]^{2+}$ with two low-spin d^8 metal ions) or with two-fold ligand-centered oxidations $[\mathbf{2^{\bullet\bullet}Cu^{II}}_2]^{2+}$ if one assumes very strong antiferromagnetic coupling between a ligand-centered radical and a Cu^{II} ion within each subunit of the molecule.

Crystals suitable for X-ray diffraction were obtained from a saturated solution of $[\mathbf{2Cu_2}](BF_4)_2$ in acetone upon slow gas phase diffusion of acetone into toluene under inert conditions. The twice oxidized species crystallizes with two additional acetone ligands, $[\mathbf{2Cu_2}(acetone)_2](BF_4)_2$, and with further solvent molecules in the crystal lattice in the same space group as neutral $\mathbf{2Cu_2}$,[15] namely *C*2/*c* (Figure 6 and SI). The dicationic character of $[\mathbf{2Cu_2}(acetone)_2]^{2+}$ is confirmed by the presence of two BF_4^- anions. While in solution D_2 symmetry was found, the solid-state symmetry is reduced to C_2. Acetone is bound as an axial ligand at long distance (d(Cu–O) = 2.39 Å), thus completing a {4 + 1} coordination sphere of each Cu ion that is reminiscent of the Jahn–Teller elongated tetragonal environment typical for d^9-Cu^{II}. In fact, according to ligand field considerations the coordination number 5 seems incompatible with ls-d^8 Cu^{III} ions. Just as in $\mathbf{2Cu_2}$, C–C bond lengths in $[\mathbf{2Cu_2}(acetone)_2]^{2+}$ reflect alternating located single and double bonds between the pyrazoles and the dipyrromethene units (see Figure S19). Most surprisingly, bond lengths do not show any significant changes compared to $\mathbf{2Cu_2}$. Also the Cu–

dx.doi.org/10.1021/ja406176e | J. Am. Chem. Soc. 2013, 135, 13892–13899

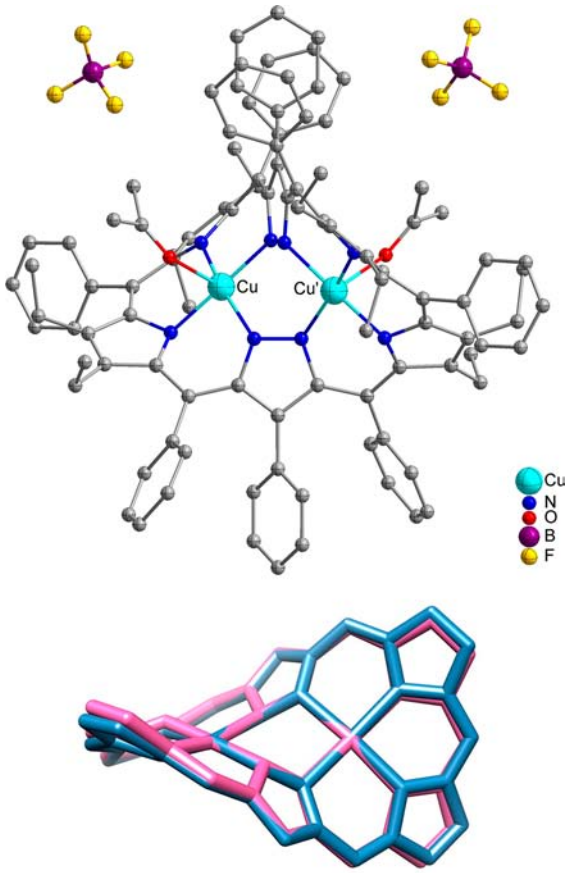

Figure 6. Top: X-ray structure of $[\mathbf{2Cu_2}(\text{acetone})_2](BF_4)_2$. Bottom: overlay of the core structures (phenyl and ethyl groups as well as H atoms omitted) of $\mathbf{2Cu_2}$ (blue) and $[\mathbf{2Cu_2}]^{2+}$ (pink).

N^{pz} bond lengths of $\mathbf{2Cu_2}$ and $[\mathbf{2Cu_2}(\text{acetone})_2]^{2+}$ (1.96 vs 1.98 Å) and the Cu–N^{pyr} bond lengths (2.00 vs 1.99 Å) differ only marginally. Consequently the overall topology of the $\mathbf{2Cu_2}$ and $[\mathbf{2Cu_2}]^{2+}$ cores is essentially identical (Figure 6, bottom). Thus metric parameters derived from X-ray crystallography do not provide any indication of either a ligand- or a metal-centered oxidation, and it appears that the dicopper complex of the Siamese-twin porphyrin is structurally invariant over several oxidation states.

XAS measurements at the Cu *K*-edge for solid $\mathbf{2Cu_2}$ and $[\mathbf{2Cu_2}(\text{acetone})_2](BF_4)_2$ finally evidenced that the copper ions in twice oxidized $[\mathbf{2Cu_2}(\text{acetone})_2]^{2+}$ remain in the +2 oxidation state. A shift of the pre-edge energy to ~2 eV higher energy is generally expected upon oxidation of Cu^{II} to Cu^{III}.[24] However, as shown in Figure 7, the pre-edge features of $\mathbf{2Cu_2}$ and $[\mathbf{2Cu_2}(\text{acetone})_2]^{2+}$ are superimposable, both occurring at ~8979.6 eV. This pre-edge energy is consistent with previously reported Cu^{II} model complexes.[24,25] The minor difference in the rising edge features of the $\mathbf{2Cu_2}$ and $[\mathbf{2Cu_2}(\text{acetone})_2]^{2+}$ spectra (at ~8986.4 and 8986.7 eV, respectively) may be attributed to subtle differences in the coordination environment (i.e., a weak axial interaction) and/or differences in covalency (i.e., due to ligand oxidation).

DFT calculations corroborated the experimental findings for two-electron oxidized $[\mathbf{2Cu_2}]^{2+}$, namely its description as $[\mathbf{2^{\bullet\bullet}Cu^{II}_2}]^{2+}$ with ligand-centered radicals. The two-electron oxidation of the complex from $\mathbf{2Cu_2}$ ($S = 1$) to $[\mathbf{2Cu_2}]^{2+}$ ($S = 2$) results in essentially no change in the spin density of the copper centers, while the spin on the ligand is increased from

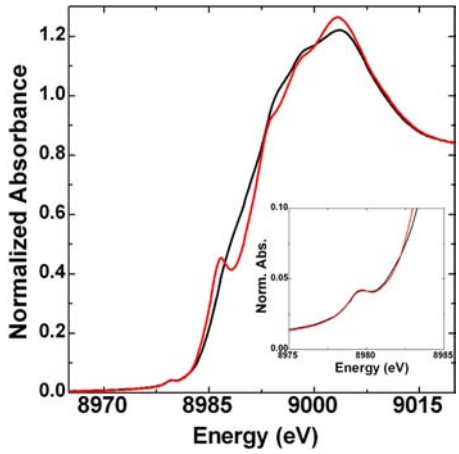

Figure 7. Cu *K*-edge XAS spectra of $\mathbf{2Cu_2}$ (red) and $[\mathbf{2Cu_2}(\text{acetone})_2](BF_4)_2$ (black). Inset: pre-edge region highlighting the 1s → 3d feature.

+1.9 to +2.7, which shows that the oxidation is purely ligand based. Since experimental findings showed that $[\mathbf{2Cu_2}]^{2+}$ has a diamagnetic ground state, the wave function was reconverged for this complex to generate the broken symmetry $S = 0$ state (calculated with B3LYP/6-311G* on the optimized triplet structure of $\mathbf{2Cu_2}$, see Figure 8 and Figure S25). In this case,

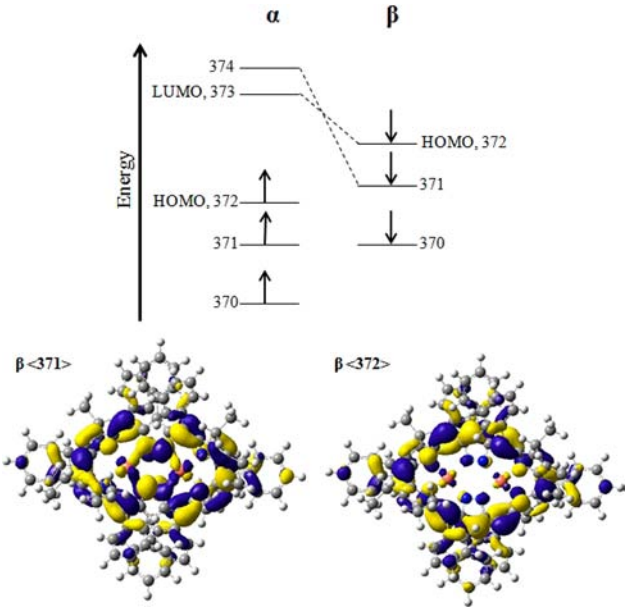

Figure 8. Top: schematic energy diagram of the frontier molecular orbitals of $[\mathbf{2Cu}]^{2+}$. Bottom: contour plots of the HOMOs ($\beta\langle 371\rangle$ and $\beta\langle 372\rangle$) for the $S = 0$ state of $[\mathbf{2Cu_2}]^{2+}$, calculated for the BP86/TZVP-optimized structure of $\mathbf{2Cu_2}$ ($S = 1$) using B3LYP/6-311G*.

the positive spin density on the copper centers does not change much, but the absolute value of the ligand spin density decreases, again due to compensation of positive and negative contributions (see above and Table S4).

Figure 8 shows the two ligand-based MOs that carry the unpaired electron density on the ligand, which therefore corresponds to a diradical. These canonical MOs are delocalized over the whole macrocycle, which at first sight seems to contradict the experimental findings, namely, the decoupling of the two subunits that was elucidated in previous

dx.doi.org/10.1021/ja406176e | J. Am. Chem. Soc. 2013, 135, 13892–13899

protonation studies of $\mathbf{2H_4}$,[17] the EPR results on $[\mathbf{2Cu_2}]^+$ (see above), and the alternating localized single- and double-bond pattern between the pyrazoles and the dipyrrine units that remains unchanged upon oxidation. Interestingly, however, one should note that simple linear combinations of these two ligand-based MOs would lead to two new MOs that are in fact localized on each side of the ring. The resulting localized MOs seem more in agreement with the experimental observations and should therefore be considered a more accurate representation of the electronic structure of $[\mathbf{Cu_2}]^{2+}$. This is illustrated in Figure 9.

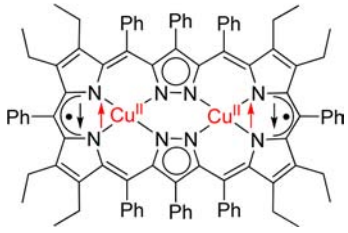

Figure 9. Simplified representation of the proposed electronic structure description of $[\mathbf{2Cu_2}]^{2+}$ that reflects the bond lengths alterations in the ligand scaffold and the twice oxidized nature of the ligand with resulting diamagnetic ground state.

Combined experimental data and DFT results therefore suggest that the Siamese-twin porphyrin serves as a redox-active ligand which, in twice oxidized $[\mathbf{2^{\bullet\bullet}Cu^{II}_2}]^{2+}$, features radical character in both subunits, while the Cu oxidation state remains invariant. Diamagnetism reflects pronounced covalency and strong antiferromagnetic coupling between the copper(II) and the ligand-based radicals. It is interesting to note that the two peripheral dipyrrin subunits of the complex Siamese-twin porphyrin framework, having an odd number of ligand atoms in the chelate ring (NCCCN, n = 5), bear resemblance to β-diketiminates, so-called NacNac$^-$ ligands, which recently have been shown to feature hidden non-innocence because of the nonbonding character of the redox-active MO.[18]

CONCLUSIONS

In summary, we present a detailed study addressing the electronic structure and the redox sites in the Siamese-twin porphyrin, which is a novel and unique expanded porphyrin providing two adjacent $\{N_4\}$ binding pockets. Here we identify this ligand as a multi-electron redox-active platform but with hidden non-innocence:[18] both $\mathbf{2Cu_2}$ and $[\mathbf{2Cu_2}]^{2+}$ have been characterized by X-ray diffraction, showing that the Siamese-twin porphyrin core is structurally invariant upon redox state changes. However, spectroscopic and DFT results reveal that in the dicopper(II) complex each subunit upon sequential oxidation forms a ligand-centered radical, though the spin vanishes because of covalency and strong antiferromagnetic coupling between the ligand radical and the proximate metal ion. In view of the increasing interest in radical ligands[26] and their use in metal-mediated catalysis,[27] complexes of the Siamese-twin porphyrin may serve as a valuable bioinspired platform that combines both metal–ligand and two-metal-ion cooperativities in multi-electron transformations of substrates. Studies in this direction have been initiated.

EXPERIMENTAL SECTION

Physical Measurements. *NMR Spectroscopy.* ^{1}H and ^{13}C NMR spectra were recorded on Bruker Avance 300 or 500 MHz spectrometers. ^{13}C NMR spectra were generally measured in proton-decoupled mode. Chemical shifts are reported in ppm relative to residual proton signals of CD_2Cl_2 at 5.32 ppm. Chemical shifts in ^{13}C NMR refer to the CD_2Cl_2 carbon atom at δ = 53.8 ppm.

UV–vis Spectroscopy. UV–vis spectra at room temperature were recorded with a Varian Cary 50 spectrometer equipped with a glass fiber optics cable and a Hellma quartz immersion probe or using quartz cuvettes (d = 1 cm). UV–vis-NIR spectra were recorded on a Varian Cary 5000 spectrophotometer. CH_2Cl_2 was used as solvent.

Magnetic Circular Dichroism (MCD). MCD data were recorded on a JASCO J-815 CD spectrometer equipped with an OXFORD SM4000 cryostat. The SM4000 cryostat employs a liquid helium-cooled superconducting magnet providing horizontal magnetic fields of 0–7 T. The J-815 spectrometer is equipped with a gaseous nitrogen-cooled xenon lamp and a detector system consisting of two interchangeable photomultiplier tubes in the UV–vis and NIR range. To obtain optical access to the sample via four optical windows made from Suprasil B quartz, the samples were loaded into a 1.5–300 K variable temperature insert. The MCD data were measured in [Θ] = mdeg and manually converted to $\Delta\varepsilon$ (M^{-1} cm^{-1} T^{-1}) using the conversion factor $\Delta\varepsilon = \Theta/(32\,980\,3\,cdB)$, with c as the concentration, B the magnetic field, and d the path length. The product cd can be replaced by $A_{MCD}/\varepsilon_{UV-vis}$, where A is the absorbance of the sample measured by the CD spectrometer. Complete spectra were recorded at different magnetic fields (0–7 T) and temperatures (2, 5, 10, 20, and 100 K) to obtain the VTVH data for all unequivocal MCD bands. This was accomplished by varying the field at a set temperature. The optical spectra were deconvoluted using the program PeakFit.

EPR Measurements. The X-band EPR spectrum of $[\mathbf{2Cu_2}]^+$ was recorded on a Bruker ELEXSYS E500 spectrometer in the temperature range of 120–298 K, equipped with a ER 049 X microwave bridge, an ER 083 CS magnet, and a digital temperature control system ER 4131 VT, and cooled with liquid nitrogen. Modulation of the microwave frequency of 9.4 GHz was performed with 5–9 G field modulation amplitude, 100 kHz field modulation frequency, and around 10 mW microwave power. The X-band EPR spectrum of $\mathbf{2Cu_2}$ was measured on Bruker E500 ELEXSYS X-band EPR spectrometer with the Bruker dual-mode cavity (ER4116DM) or a standard cavity (ER4102ST) and an Oxford Instruments helium flow cryostat (ESR 910). Microwave frequencies were measured with a Hewlett-Packard frequency counter (HP5352B), and the field control was calibrated with a Bruker NMR field probe (ER035M). The EPR spectrum of $\mathbf{2Cu_2}$ was simulated using ESIM developed by E. Bill, the one for $[\mathbf{2Cu_2}]PF_6$ was simulated using the XSophe–Sophe-XeprView[28] software. Usually full matrix diagonalization was applied with the SOPHE interpolation scheme for field and angular space; two field segments and an angular grid of 40 bands were sufficient for good reproducible results. As the dimeric structure of $\mathbf{2Cu_2}$ is well established,[16,17] the simulation was run with a two spin system instead of a triplet model, in order to take the twist of the magnetic axes for the bimetallic system with rhombic symmetry for each copper ion according to the C_2-symmetric relation of the two subunits into account (see Results and Discussion section). Locally, the same set of parameters was used for each copper(II) ion with best results found at $\mathbf{g}$ = (2.03, 2.07, 2.13) and $\mathbf{A}$ = (0, 0, 220)·10^{-4} cm^{-1}. To model the twist of the coordinate system and to optimize the simulation, the $\mathbf{g}$-tensor for the Cu(2) site has been rotated by 90° around the x-axis and the and $\mathbf{A}$-tensor by 80°. The isotropic coupling between the two cores was set to J = +8 cm^{-1} (whereby the shape of the spectrum is independent of the value for J if $|J| > 1$ cm^{-1}). The traceless tensor of the dipole coupling, given in the axis system of Cu(1) was found to be $\mathbf{J}_d$ = (251, 442, −694)·10^{-4} cm^{-1} using a spin-coupling Hamiltonian defined as $\hat{H} = \hat{S}_1\cdot(2J\cdot\mathbf{1} + Jd)\,\hat{S}_2$, where $\mathbf{1}$ is the unity matrix. The isotropic line width was set to 40 × 10^{-4} cm^{-1}, and Lorentzian line shapes were applied. Simplifying the two rhombic spin centers to dipoles and the application of a simple dipole–dipole model determined the metal–metal separation to be 3.8 Å. This value agrees

well with the metal−metal separation of 3.88 Å found from X-ray data analysis. Allowed transitions at $g = 2$ and half-field signals at $g = 4$ have been consistently simulated using the same set of parameters; only for $B_1 \| B_0$, the settings in the simulation program were changed from perpendicular to parallel mode.

Electrochemical Measurements. Redox properties were studied by CV, SWV, and bulk electrolysis in CH_2Cl_2/0.1 M $[NBu_4]PF_6$ (electrochemical grade) solutions using a PerkinElmer 263A potentiostat controlled by electrochemistry powersuit software. For CV and SWV, a glassy carbon electrode was used as working electrode, platinum as counter electrode, and silver as reference electrode. For bulk electrolysis measurements, a platinum net was used as working electrode, reference and counter electrode remained the same. CV and SWV spectra were measured versus decamethylferrocene as internal standard and then referenced to ferrocene.

X-ray Absorption Spectroscopy. Solid samples diluted in boron nitride were measured at SSRL (Stanford Synchrotron Radiation Lightsource, 3 GeV ring) beamline 7-3 equipped with a Si(220) double crystal monochromator for energy selection. Data were collected in transmission mode. Data averaging and energy calibration were performed using SixPack.[29] For energy calibration, the first inflection point from the XANES spectral region of a Cu foil was set to 8980.3 eV. The AUTOBK algorithm available in the Athena software package was employed for data reduction and normalization.[30]

X-ray Crystallography. X-ray data for $[\mathbf{2Cu_2}(acetone)_2](BF_4)_2 \cdot 2$ toluene·2 acetone were collected on a STOE IPDS II diffractometer (graphite monochromated Mo−K_α radiation, $\lambda = 0.71073$ Å) by use of ω scans. The structure was solved by direct methods and refined on F^2 using all reflections with SHELX.[31] Most nonhydrogen atoms were refined anisotropically. Hydrogen atoms were placed in calculated positions and assigned to an isotropic displacement parameter of 1.2/1.5 *U*eq(C). Counterions and toluene solvent molecules were found to be disordered. SADI (*d*B−F, *d*F−F) restraints and EADP constraints were used to model the disorder of the counterions; SADI, SIMU, DELU, ISOR restraints as well as the AFIX 66 instruction and one EADP constraint for the disordered toluene.

Materials and Synthetic Procedures. $\mathbf{2Cu_2}$ was prepared as reported previously.[16,17] Starting materials and solvents were purchased either from abcr, Sigma Aldrich or Acros; solvents were dried according to established procedures.

$[\mathbf{2Cu_2}]BF_4$. To a solution of $\mathbf{2Cu_2}$ (28 mg, 20 μmol) in CH_2Cl_2 (15 mL) 1 equiv of $AgBF_4$ (200 μL, 0.1 M stock solution in $EtNO_2$) was added, and the reaction monitored via UV−vis spectroscopy. The solvent was removed under reduced pressure, and the remaining solid redissolved in 10 mL CH_2Cl_2. The suspension was filtered at air using a membrane filter. The solvent was removed under reduced pressure, and the product $[\mathbf{2Cu_2}]BF_4$ had to be stored under inert conditions (yield 96%). UV−vis ν (ε): 16 529 (2.5), 23 753 (3.6), 25 773 (3.6), 30 769 (2.5) cm^{-1} (10^4 M^{-1} cm^{-1}).

$[\mathbf{2Cu_2}](BF_4)_2$. To a solution of $\mathbf{2Cu_2}$ (28 mg, 20 μmol) in CH_2Cl_2 (15 mL) 2 equiv of $AgBF_4$ (400 μL, 0.1 M stock solution in $EtNO_2$) were added, and the reaction monitored via UV−vis spectroscopy. The solvent was removed under reduced pressure, and the remaining solid redissolved in 10 mL CH_2Cl_2. The suspension was filtered at air using a membrane filter. The solvent was removed under reduced pressure, and the product $[\mathbf{2Cu_2}](BF_4)_2$ had to be stored under inert conditions (97%). Single crystals of $[\mathbf{2Cu_2}(acetone)_2](BF_4)_2 \cdot 2$ toluene·2 acetone were obtained by slow evaporation of acetone from a saturated solution of $[\mathbf{2Cu_2}](BF_4)_2$ in acetone into toluene under inert conditions. ^{1}H NMR (300 MHz, CD_2Cl_2) δ: 8.08 (d, 4H), 8.00 (t, 2H), 7.41−7.55 (m, 12H), 7.28 (t, 4H), 6.92 (t, 4H), 6.80 (t, 4H), 6.68 (t, 2H), 6.56 (t, 4H), 6.48 (d, 4H), 1.99−2.29 (m, 12H, CH_2), 1.56−1.73 (m, 4H, CH_2), 0.69 (t, 12H, CH_3), 0.67 (t, 12H, CH_3) ppm; ^{13}C NMR (125 MHz, CD_2Cl_2) δ: 179.5, 174.6, 167.0, 157.3, 151.7, 144.6, 140.5, 136.2, 132.0, 130.1, 129.9, 129.3, 129.2, 128.6, 128.4, 128.3, 127.2, 127.1, 126.8, 124.8, 19.7 (CH_2), 19.2 (CH_2), 15.8 (CH_3), 15.7 (CH_3) ppm; UV−vis ν (ε): 16 863 (2.2), 17 986 (2.4), 23 095 (3.9), 25 316 (3.2), 31 056 (2.6), 36 232 (2.9) cm^{-1} (10^4 M^{-1} cm^{-1}).

DFT Calculations. The structure of $\mathbf{2Cu_2}$ was fully optimized for the $S = 1$ ground state and the broken-symmetry ($S = 0$) state using the BP86[32] functional and TZVP[33] basis set. Single point energies on these structures were also calculated using the B3LYP functional[32b,34] and the TZVP basis set. In order to investigate the properties of the one- and two-electron oxidized cations $[\mathbf{2Cu_2}]^+$ and $[\mathbf{2Cu_2}]^{2+}$, the BP86/TZVP-optimized structure of $\mathbf{2Cu_2}$ in the triplet ground state was used. Wave functions were then converged for the $S = 3/2$ state and the broken-symmetry $S = 1/2$ state of the cation and the $S = 2$ state and the broken-symmetry $S = 0$ state of the dication using the B3LYP functional and the 6-311G* basis set. All of these calculations were performed using the program package Gaussian 03.[35] TD-DFT calculations were performed for the triplet ground state of $\mathbf{2Cu_2}$ on the corresponding BP86/TZVP-optimized structure using B3LYP/def2-SV(P). These calculations were performed using ORCA.[36]

■ ASSOCIATED CONTENT

Supporting Information

Synthetic procedures and complete experimental details; crystallographic details (CIF) for $[\mathbf{2Cu_2}(acetone)_2](BF_4)_2$; spectroscopic and magnetic data (EPR, UV−vis, MCD, NMR) as well as electrochemical and spectroelectrochemical data; details on DFT calculations. This material is available free of charge via the Internet at http://pubs.acs.org.

■ AUTHOR INFORMATION

Corresponding Authors

serena.debeer@cec.mpg.de
lehnertn@umich.edu
franc.meyer@chemie.uni-goettingen.de

Notes

The authors declare no competing financial interest.

■ ACKNOWLEDGMENTS

Financial support from the Fonds der Chemischen Industrie (Ph.D. scholarship to L.K.B.), from Georg-August-University as well as from the Max Planck Society is gratefully acknowledged. Portions of the research were carried out at the Stanford Synchrotron Radiation Lightsource (SSRL), a national user facility operated by Stanford University on behalf of the DOE, BES. The SSRL SMB Program is supported by DOE, BER and NIH, NCRR, BMTP.

■ REFERENCES

(1) (a) Stillman, M. J. *J. Porphyrins Phthalocyanines* **2000**, *4*, 374−376. (b) Scheidt, W. R. *J. Biol. Inorg. Chem.* **2001**, *6*, 727−732.

(2) Bertini, I.; Gray, H. B.; Stiefel, E. I.; Valentine, J. S. *Biological Inorganic Chemistry*; University Science Books: Sausalito, CA, 2007.

(3) Borg, D. C.; Fajer, J.; Felton, R. H.; Dolphin, D. *Proc. Natl. Acad. Sci. U.S.A.* **1970**, *67*, 813−820.

(4) Felton, R. H.; Davis, D. G. In *The Porphyrins*; Dolphin, D., Ed.; Academic Press: New York, 1978.

(5) Kadish, K. M.; v. Caemelbecke, E.; Royal, G.In *The Porphyrin Handbook*; Kadish, K. M., Smith, K. M., Guilard, R., Eds.; Academic Press: San Diego, CA, 2000; Vol. *8*.

(6) (a) Sessler, J. L.; Gebauer, A.; Weghorn, S. J. In *The Porphyrin Handbook*; Kadish, K. M., Smith, K. M., Guilard, R., Eds.; Academic Press: San Diego, CA, 2000; Vol. *2*. (b) Saito, S.; Osuka, A. *Angew. Chem., Int. Ed.* **2011**, *50*, 4342−4373. (c) Stępień, M.; Sprutta, N.; Latos-Grażyński, L. *Angew. Chem., Int. Ed.* **2011**, *50*, 4288−4340.

(7) Stanienda, A. *Z. Phys. Chem.* **1962**, *33*, 170−180.

(8) (a) Sessler, J. L.; Tomat, E. *Acc. Chem. Res.* **2007**, *40*, 371−379. (b) Sessler, J. L.; Vivian, A. E.; Seidel, D.; Burrell, A. K.; Hoehner, M.; Mody, T. D.; Gebauer, A.; Weghorn, S. J.; Lynch, V. *Coord. Chem. Rev.* **2001**, *216−217*, 411−434.

(9) Mayer, I.; Nakamura, K.; Srinivasan, A.; Furuta, H.; Toma, H. E.; Araki, K. *J. Porphyrins Phthalocyanines* **2005**, *09*, 813−820.
(10) (a) Kang, S.; Hayashi, H.; Umeyama, T.; Matano, Y.; Tkachenko, N. V.; Lemmetyinen, H.; Imahori, H. *Chem. Asian J.* **2008**, *3*, 2065−2074. (b) Sintic, P. J.; Ou, W. E. Z.; Shao, J.; McDonald, J. A.; Cai, Z.-L.; Kadish, K. M.; Crossley, M. J.; Reimers, J. R. *Phys. Chem. Chem. Phys.* **2008**, *10*, 268−280.
(11) (a) Charriere, R.; Jenny, T. A.; Rexhausen, H.; Gossauer, A. *Heterocycles* **1993**, *36*, 1561−1575. (b) Suzuki, M.; Osuka, A. *Org. Lett.* **2003**, *5*, 3943−3946. (c) Sankar, J.; Mori, S.; Saito, S.; Rath, H.; Suzuki, M.; Inokuma, Y.; Shinokubo, H.; Kim, K. S.; Yoon, Z. S.; Shin, J.-Y.; Lim, J. M.; Matsuzaki, Y.; Matsushita, O.; Muranaka, A.; Kobayashi, N.; Kim, D.; Osuka, A. *J. Am. Chem. Soc.* **2008**, *130*, 13568−13579.
(12) Mori, S.; Osuka, A. *J. Am. Chem. Soc.* **2005**, *127*, 8030−8031.
(13) Mori, S.; Shimizu, S.; Shin, J.-Y.; Osuka, A. *Inorg. Chem.* **2007**, *46*, 4374−4376.
(14) (a) Shimizu, S.; Anand, V. G.; Taniguchi, R.; Furukawa, K.; Kato, T.; Yokoyama, T.; Osuka, A. *J. Am. Chem. Soc.* **2004**, *126*, 12280−12281. (b) Suzuki, M.; Yoon, M.-C.; Kim, D. Y.; Kwon, J. H.; Furuta, H.; Kim, D.; Osuka, A. *Chem.—Eur. J.* **2006**, *12*, 1754−1759. (c) Koide, T.; Furukawa, K.; Shinokubo, H.; Shin, J.-Y.; Kim, K. S.; Kim, D.; Osuka, A. *J. Am. Chem. Soc.* **2010**, *132*, 7246−7247.
(15) (a) Srinnivasan, A.; Ishizuka, T.; Osuka, A.; Furuta, H. *J. Am. Chem. Soc.* **2003**, *125*, 878−879. (b) Gokulnath, S.; Yamaguchi, K.; Toganoh, M.; Mori, S.; Uno, H.; Furuta, H. *Angew. Chem.* **2011**, *123*, 2350−2354.
(16) Frensch, L. K.; Pröpper, K.; John, M.; Demeshko, S.; Brückner, C.; Meyer, F. *Angew. Chem., Int. Ed.* **2011**, *50*, 1420−1424.
(17) Blusch, L. K.; Hemberger, Y.; Pröpper, K.; Dittrich, B.; Witterauf, F.; John, M.; Bringmann, G.; Brückner, C.; Meyer, F. *Chem.—Eur. J.* **2013**, *19*, 5868−5880.
(18) Khusniyarov, M. M.; Bill, E.; Weyhermüller, T.; Bothe, E.; Wieghardt, K. *Angew. Chem., Int. Ed.* **2011**, *50*, 1652−1655.
(19) (a) Cheeseman, M. R.; Greenwood, C.; Thomson, A. J. *Adv. Inorg. Chem.* **1991**, *36*, 201−255. (b) Mack, J.; Stillman, M. J.; Kobayashi, N. *Coord. Chem. Rev.* **2007**, *251*, 429−453. (c) Lehnert, N. *J. Inorg. Biochem.* **2012**, *110*, 83−93.
(20) (a) Paulat, F.; Lehnert, N. *Inorg. Chem.* **2008**, *47*, 4963−4976. (b) Galinato, M. G. I.; Spolitak, T.; Ballou, D. P.; Lehnert, N. *Biochemistry* **2011**, *50*, 1053−1069.
(21) (a) Barkigia, K. M.; Chantranupong, L.; Smith, K. M.; Fajer, J. *J. Am. Chem. Soc.* **1988**, *110*, 7566−7567. (b) Barkigia, K. M.; Renner, M. W.; Furenlid, L. R.; Medforth, C. J.; Smith, K. M.; Fajer, J. *J. Am. Chem. Soc.* **1993**, *115*, 3627−3635.
(22) (a) Heinze, J. *Angew. Chem., Int. Ed.* **1984**, *23*, 831−847. (b) Kaim, W.; Klein, A.; Glöckle, M. *Acc. Chem. Res.* **2000**, *33*, 755−763.
(23) (a) Song, H.; Reed, C. A.; Scheidt, W. R. *J. Am. Chem. Soc.* **1989**, *111*, 6865−6866. (b) Erler, B. S.; Scholz, W. F.; Lee, Y. J.; Scheidt, W. R.; Reed, C. A. *J. Am. Chem. Soc.* **1987**, *109*, 2644−2652. (c) Renner, M. W.; Barkigia, K. M.; Zhang, Y.; Medforth, C. J.; Smith, K. M.; Fajer, J. *J. Am. Chem. Soc.* **1994**, *116*, 8582−8592.
(24) (a) DuBois, J. L.; Mukherjee, P.; Stack, T. D. P.; Hedman, B.; Solomon, E. I.; Hodgson, K. O. *J. Am. Chem. Soc.* **2000**, *122*, 5775−5787. (b) Sarangi, R.; Aboelella, N.; Fujisawa, K.; Tolman, W. B.; Hedman, B.; Hodgson, K. O.; Solomon, E. I. *J. Am. Chem. Soc.* **2006**, *128*, 8286−8296.
(25) Kau, L. S.; Spira-Solomon, D. J.; Penner-Hahn, J. E.; Hodgson, K. O.; Solomon, E. I. *J. Am. Chem. Soc.* **1987**, *109*, 6433−6442.
(26) (a) Chaudhuri, P.; Wieghardt, K. *Prog. Inorg. Chem.* **2001**, *50*, 151−216. (b) Ray, K.; Petrenko, T.; Wieghardt, K.; Neese, F. *Dalton Trans.* **2007**, *16*, 1552−1566. (c) Kaim, W. *Eur. J. Inorg. Chem.* **2012**, 343−348.
(27) (a) Chirik, P. J.; Wieghardt, K. *Science* **2010**, *327*, 794−795. (b) Dzik, W. I.; de Bruin, B. *Organomet. Chem.* **2011**, *37*, 46−78. (c) Praneeth, V. K. K.; Ringenberg, M. R.; Ward, T. R. *Angew. Chem., Int. Ed.* **2012**, *51*, 10228−10234.
(28) (a) Heichel, M.; Höfer, P.; Kamlowski, A.; Griffin, M. M.; Noble, C. A.; Wang, D.; Hanson, G. R.; Eldershaw, C.; Gates, K. E.; Burrage, K. *Bruker Report* **2000**, *148*, 6−9. (b) Hanson, G. R.; Gates, K. E.; Noble, C. J.; Griffin, M.; Mitchell, A.; Benson, S. *J. Inorg. Biochem.* **2004**, *98*, 903−916.
(29) Webb, S. M. *Phys. Scr.* **2005**, *T115*, 1011−1014.
(30) Ravel, B.; Newville, M. *J. Synchrotron Radiat.* **2005**, *12*, 537−541.
(31) Sheldrick, G. M. *Acta Crystallogr.* **2008**, *A64*, 112−122.
(32) (a) Perdew, J. P. *Phys. Rev. B* **1986**, *33*, 8822−8824. (b) Becke, A. D. *Phys. Rev. A* **1988**, *38*, 3098−3100.
(33) (a) Schaefer, A.; Horn, H.; Ahlrichs, R. *J. Chem. Phys.* **1992**, *97*, 2571−2577. (b) Schaefer, A.; Huber, C.; Ahlrichs, R. *J. Chem. Phys.* **1994**, *100*, 5829−5835.
(34) (a) Becke, A. D. *J. Chem. Phys.* **1993**, *98*, 1372−1377. (b) Becke, A. D. *J. Chem. Phys.* **1993**, *98*, 5648−5652.
(35) Frisch, M. J.; Trucks, G. W.; Schlegel, H. B.; Scuseria, G. E.; Robb, M. A.; Cheeseman, J. R.; Montgomery, J. A., Jr.; Vreven, T.; Kudin, K. N.; Burant, J. C.; Millam, J. M.; Iyengar, S. S.; Tomasi, J.; Barone, V.; Mennucci, B.; Cossi, M.; Scalmani, G.; Rega, N.; Petersson, G. A.; Nakatsuji, H.; Hada, M.; Ehara, M.; Toyota, K.; Fukuda, R.; Hasegawa, J.; Ishida, M.; Nakajima, T.; Honda, Y.; Kitao, O.; Nakai, H.; Klene, M.; Li, X.; Knox, J. E.; Hratchian, H. P.; Cross, J. B.; Bakken, V.; Adamo, C.; Jaramillo, J.; Gomperts, R.; Stratmann, R. E.; Yazyev, O.; Ausin, A. J.; Cammi, R.; Pomelli, C.; Octerski, J. W.; Ayala, P. Y.; Morokuma, K.; Voth, G. A.; Salvador, P.; Dannenberg, J. J.; Zakrzewski, V. G.; Dapprich, S.; Daniels, A. D.; Strain, M. C.; Farkas, O.; Makick, D. K.; Rabuck, A. D.; Raghavachair, K.; Foresman, J. B.; Ortiz, J. V.; Cui, Q.; Baboul, A. G.; Clifford, S.; Cioslowski, J.; Stefanov, B. B.; Lui, G.; Laishenko, A.; Piskorz, R.; Komaromi, I.; Martin, R. L.; Fox, D. J.; Keith, T.; Al-Laham, M. A.; Peng, C. Y.; Nanayakkara, A.; Challacombe, M.; Gill, P. M. W.; Johnson, B.; Chen, W.; Wong, M. W.; Gonzalez, C.; Pople, J. A. *Gaussian 09*; Gaussian, Inc.: Pittsburgh, PA, 2003.
(36) Neese, F.; *ORCA*; Max-Planck Institut für Chemische Energiekonversion: Muelheim/Ruhr, Germany, 2012.